# 行政院國家科學委員會專題研究計畫　成果報告

## 由奈米組件建構三維人造晶體的光電特性與量子態控制

計畫類別：個別型計畫
計畫編號：NSC94-2112-M-009-031-
執行期間：94 年 08 月 01 日至 95 年 07 月 31 日
執行單位：國立交通大學光電工程學系(所)

計畫主持人：黃中垚

報告類型：精簡報告
報告附件：出席國際會議研究心得報告及發表論文
處理方式：本計畫可公開查詢

中　華　民　國 95 年 5 月 22 日

# 行政院國家科學委員會補助專題研究計畫 □ 成 果 報 告 v 期中進度報告

## 由奈米組件建構三維人造晶體的光電特性與量子態控制（I）

## Photoelectric properties and quantum control of three-dimensional artificial crystals assembly from a variety of nanometers building blocks (I)

計畫類別：v 個別型計畫　　□ 整合型計畫

計畫編號：NSC 94-2112-M-009 -031-

執行期間：94 年 08 月 01 日至 95 年 07 月 31 日

計畫主持人：黃中垚
共同主持人：
計畫參與人員：

成果報告類型(依經費核定清單規定繳交)：v 精簡報告　□完整報告

本成果報告包括以下應繳交之附件：
□赴國外出差或研習心得報告一份
□赴大陸地區出差或研習心得報告一份
v 出席國際學術會議心得報告及發表之論文各一份
□國際合作研究計畫國外研究報告書一份

處理方式：除產學合作研究計畫、提升產業技術及人才培育研究計畫、列管計畫及下列情形者外，得立即公開查詢
□ 涉及專利或其他智慧財產權，□一年□二年後可公開查詢
□

執行單位：國立交通大學光電工程研究所

中　華　民　國 95 年 5 月 31 日

**中文摘要**

此三年期計畫之主要目的在研究各式奈米組件所構裝出之新型人造材料的光電特性。我們將使用二維光譜與量子態控制技術研究三維人造材料光激動態與衰退機制。

第一年我們首先探討下列三種奈米組件構裝出之新型材料之應用特性，以為下階段量子態控制研究之基礎: (一)以高密度三維分佈的矽、鍺奈米量子點發展出新奇奈米結構矽基鐵電材料。實驗證實此新型材料之特性源自矽奈米晶粒之介面缺陷態捕捉電荷產生自發極矩，此材料之鐵電特性之 Curie temperature 高達 195 $^{o}$C。其極矩約為傳統鈣鈦礦鐵電材料極矩之十分之一。(二) 摻雜氧化鋅奈米微晶之強誘電性液晶材料，發現氧化鋅奈米組件具有捆綁分子能力，可增進強誘電性液晶分子之靜態與動態排列，有效改善強誘電性液晶分子之應用特性。 (三)以溶液成長法製備磁性材料/貴金屬核-殼量子點結構，並製備成週期排列自動組裝三維奈米結構薄膜。

**Abstract**

We propose in this project to investigate photoelectric properties of three-dimensional artificial crystals assembling from a variety of nano building blocks. We plan to apply 2D spectroscopy and quantum control technique to probe the structural dynamics of the photoexcited artificial crystals.

In this first-year progress report, we present some pioneering studies on following three new nanostructured materials: (I) a room-temperature ferroelectric with a three-dimensional array of Si (or Ge) nanocrystals embedded in a mesoporous silica matrix. The ferroelectric effect is attributed to electrical dipole layers lying between nanocrystals and the silica host. The resulting remnant polarization is as large as one-tenth that of typical multi-element perovskite ferroelectrics. (II) We found that the molecular alignment of FLC in steady-state or in dynamic state can be improved by doping with ZnO nanocrystals. ZnO nano building blocks serve as molecular binders to enhance the application properties of ferroelectric liquid crystal molecules. (III) Magnetic/noble metal core-shell quantum dots prepared with solution growth technique has been developed to building highly ordered self-assembling bulk film. This progress offers an opportunity to probe and control the photo-carriers transport dynamics in a low-dimensional quantum-confined system.

**Progress Report**

This project, which had been supported by NSC in the past one year, has produced very promising results, which include the demonstrations of

## (I) Novel silicon-based ferroelectric material with a three-dimensional array of Si (or Ge) nanocrystals embedded in a mesoporous silica matrix

Ferroelectric materials (1-2) have been widely used in applications such as sensors (3), actuators (4), and nonvolatile memory devices (5-6). For example, ferroelectric random-access memories (FERAM) could in principle operate at nanosecond read/write speed, exhibit long retention time, and allow almost unlimited number of operation cycles (6). The spontaneous polarization of a ferroelectric material is mainly due to dipoles that can switch directions under the influence of an electric field. The nonvanishing electrical polarization is a result of the non-centrosymmetric crystal structure. Bulk silicon does not possess ferroelectric properties because it is of the diamond structure. No net dipolar polarization is produced by the displacement of ions in the crystal lattice. Tremendous efforts have been made to integrate non-silicon-based ferroelectric films, such as lead zirconate titanate (PZT) (2, 6), with the mature silicon-based memory technology to realize FERAM. However, the interface reactions between PZT and the Si substrate, which results in mobile ions and low retention, make it difficult to obtain a good ferroelectric/Si interface. Contamination of the Si integrated circuit (IC) fabrication line by metal ions in a non-Si based ferroelectric is also a major concern (1). The development of silicon-based ferroelectric thin films will enable the realization of FERAM that is IC-compatible.

At the nanometer scale, the ratio of the numbers of atoms on the surface and in the bulk of a material increases rapidly. Interfacial properties of a nanostructured material could, therefore, enable new functional devices (7-8). In this regard, self-assembled mesoporous silica (MS) (9-10) is attractive for its extremely large internal surface area and controllable nanoporous structure. For example, enhanced blue photoluminescence (PL) in three-dimensional Si nanocrystals (nc) embedded in MS had been reported (11). In this report, we present that effect dominated by interface of nc-Si embedded MS can serve as new silicon-based non-perovskite ferroelectric.

The test samples were prepared by first depositing a 5-nm-thick $SiO_2$ buffer layer and then spin coating an 85-nm thick MS nanotemplate layer on a *p*-type silicon substrate. Si or Ge nanocrystals were thereafter synthesized in the MS templates by using the high-density inductively coupled plasma (ICP) method (11-12). During the synthesis, we applied a negative voltage of 40 V at 300 kHz on the substrate. This creates preferential growth of nc-Si on the bottom of the pore-channels (12), as illustrated in Fig. 1 (A). Finally a 10-nm-thick $SiO_2$ layer was deposited on the MS films and then electrode is formed to complete a metal-oxide-silicon (MOS) structure for capacitance-voltage (C-V) and polarization-electric field (P-E) measurements.

Figure I-1(B) shows the cross-sectional TEM image of a typical MS film with silicon nanocrystals. The distinct lattice fringes shown in the inset of Fig. I-1(B) indicates high

crystalline quality of the Si nanocrystals. By analyzing the transmission electron microscopy (TEM) images and the concentration profiles of specific atoms from secondary ion mass spectroscopy, the average sizes of nc-Si were found to be 4 nm, 5 nm, and 5 nm for the samples with high ($2.5\times10^{18}$), moderate ($5\times10^{17}$) and low ($1.5\times10^{17}cm^{-3}$) number densities of nc-Si, respectively. Germanium nanocrystals with similar densities can also be obtained under identical sample preparation conditions. This indicates similar growth mechanism for both silicon and germanium in MS matrix.

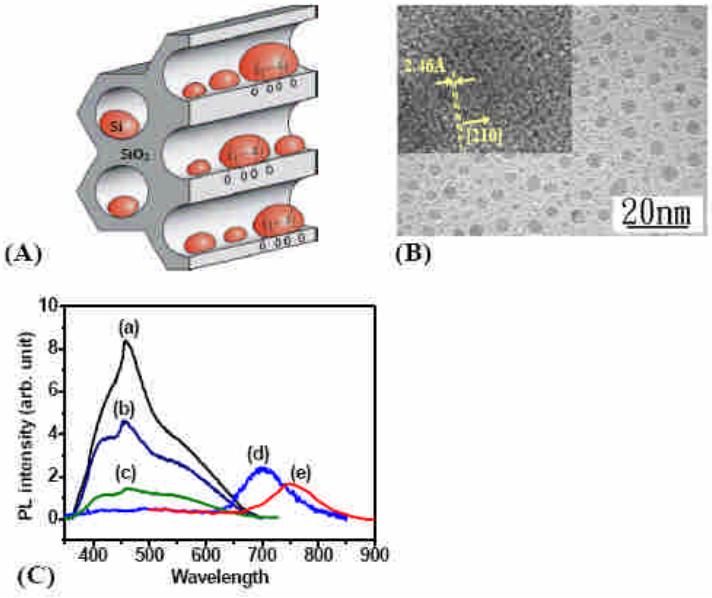


**Fig. I-1**: (A) A schematic drawing illustrating the one-side bonding geometry of Si nanocrystals in porechannels prepared by applying an electric field during the synthesis process. (B) The cross-sectional TEM images of the mesoporous silica (MS) films with high density silicon nanocrystals and the observed distinct lattice fringes shown in the inset. (C) Photo-luminescence (PL) spectra of (a) high, (b) moderate, (c) low density nc-Si embedded MS films; and (d) high, (e) moderate density nc-Si embedded mesoporous silica samples thermally annealed at 1000 $^{o}$C for 2 hours.

The photoluminescence (PL) spectra of these nanostructured films shown in Figure I-1(C) exhibit a broad-band emission at 2.7 eV ($\lambda$=460 nm) for all as-grown samples with a peak intensity increasing with the number density of nc-Si. After thermal annealing, the peak disappeared while a new luminescence band around 1.77 eV ($\lambda$~700 nm) of which the peak wavelength depends on the size of nc-Si was observed. Since the short-wavelength PL peak at 460 nm was also observed on pure MS template (11, 13) and nc-Ge-embedded MS (11), we attribute the blue PL emission to the interfacial states associated with neutral defects of oxygen vacancy (≡Si-Si≡) (14) in the MS matrix. The semiconductor nanocrystals, however, also play a role by sensitizing the blue emission through generating more photoexcited carriers. These carriers are then trapped in the interfacial oxygen defects and recombine to increase the intensity of the peak 460-nm PL. Thermal annealing effectively removes these defects and leads to a formation of isolated nanocrystals. The PL peak at 700 nm comes from band-to-band recombination of the isolated nanocrystals and therefore exhibits quantum-confined size-effect (15). From the observed wavelength shift, we estimate the Si nanocrystals to be about 4-5 nm in dimension, in agreement with the TEM observation.

The issue relating to the change of bonding configurations after annealing was analyzed with X-ray photoemission spectroscopy (XPS). However, to separate signal from nanocrystals to that

from the MS background, we also synthesized nc-Ge instead of nc-Si in the MS, as Si and Ge nanocrystals are known to undergo similar growth process in MS matrix (11). The measured spectra of the Ge-3*d* core level (1455 eV, the Ge-Ge bond geometry) and its chemical shift due to the existence of chemical bonds of Ge-O (1452 eV) (16) are presented in Figure I-2(A). From the ratio of the areas of two deconvoluted peaks, I(Ge-O)/I(Ge-Ge), before and after thermal annealing, we can conclude that thermal annealing effectively breaks the bonding of nc-Ge with the MS host. The interfacial structure formed by Ge-O or Si-O is thus altered by annealing to render the embedded nanocrystals into isolated quantum dots.

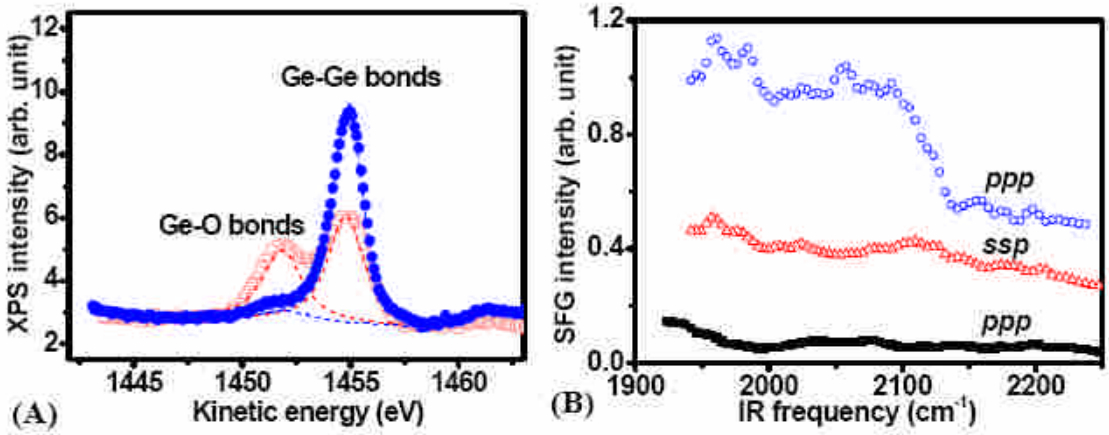


**Fig. I-2:** (A) XPS spectra of moderate density nc-Ge embedded mesoporous silica film before (open squares) and after annealing (solid circles). (B) Sum-frequency signal from MS (filled symbols) and as-grown nc-Si embedded MS films (open symbols) prepared with bias of -40 V during the ICP growth cycle are presented as a function of infrared frequency. Here ppp and ssp (from left to right) denote the beam polarization directions of sum-frequency beam at 480 nm, visible-beam at 532 nm and infrared frequency to be either *p*-polarized (lying on the incident plane) or *s*-polarized (perpendicular to the incident plane).

We apply optical sum-frequency generation (SFG) to verify the existence and magnitude of optical polarization in this novel material by taking advantage of the sensitivity of SFG to polar structure of molecular bonding geometry (17). The SFG spectra of MS and as-grown nc-Si embedded MS films prepared with bias of -40V during ICP growth cycle are presented in Fig. I-2(B). The samples were excited by 20-ps, pulses at $\lambda$=532 nm and synchronous infrared pulses tunable from 5 μm to 6 μm. The reflected SFG signal at about 480 nm was recorded as a function of the infrared wavelength with various combinations of the beam polarizations. Broad resonance was detected as the infrared pulse was tuned to below 2150 $cm^{-1}$ and the resonance persists to 1950 $cm^{-1}$. The resonance can be attributed to the overtone of Si=O stretch mode. The broad resonance feature suggests the chemical bonds to be extremely complex with various bonding geometries at the interfaces of nc-Si and MS. The *s*-polarized SFG signal is much weaker than that of *p*-polarized signal, suggesting the polar bonding structure to be essentially perpendicular to the film surface. By comparing to the reflected SFG signal from that of a z-cut $LiNbO_3$ plate under the same excitation level and beam geometry, we estimate the SFG susceptibility of the as-grown nc-Si embedded MS film to be $d^{(2)}_{ppp}$=3.8 pm/V. This value is about the averaged magnitude of second-order nonlinear optical responses of all ferroelectric crystals currently known.

The electrical properties of nc-Si embedded MS were studied in a MOS capacitor configuration. The results are summarized in Fig. I-3(A). We note two key features in these C-V

curves. First, clockwise hysteretic loops present in all MOS capacitors of as-grown nc-Si embedded MS films (See curves *a*-*c* of Fig. I-3 (A)). Note that charging (discharging) of QDs by electrons (holes) via a tunneling process shifts the flat-band voltage to a more (less) positive value (18). This shall lead to a counter-clockwise C-V loop when a positive-to-negative-to-positive voltage sweep is carried out, which contradicts with what we had observed. Second, the leakage current through the $SiO_2$/nc-Si–embedded-MS/$SiO_2$ stack of our samples is extremely low with a magnitude of $1.0\times10^{-7}$ A/cm$^2$ at $1\times10^6$ V/cm, indicating a very low tunneling current in our samples. The C-V characteristic curve of a MOS capacitor becomes counter-clockwise when the nc-Si embedded MS insulation layer is annealed (see curve *d* of Fig. I-3(A)). Therefore the observed clockwise C-V hysteretics of our MOS capacitors with as-grown nc-Si embedded MS are unlikely to originate from charge localization in the embedded dots (19), but from an electrical polarization layer (20). Depending on the direction of the applied electric field, the build-in dipole field of the sample would either enhance or screen the external field, resulting in the observed C-V hysteretic loop.

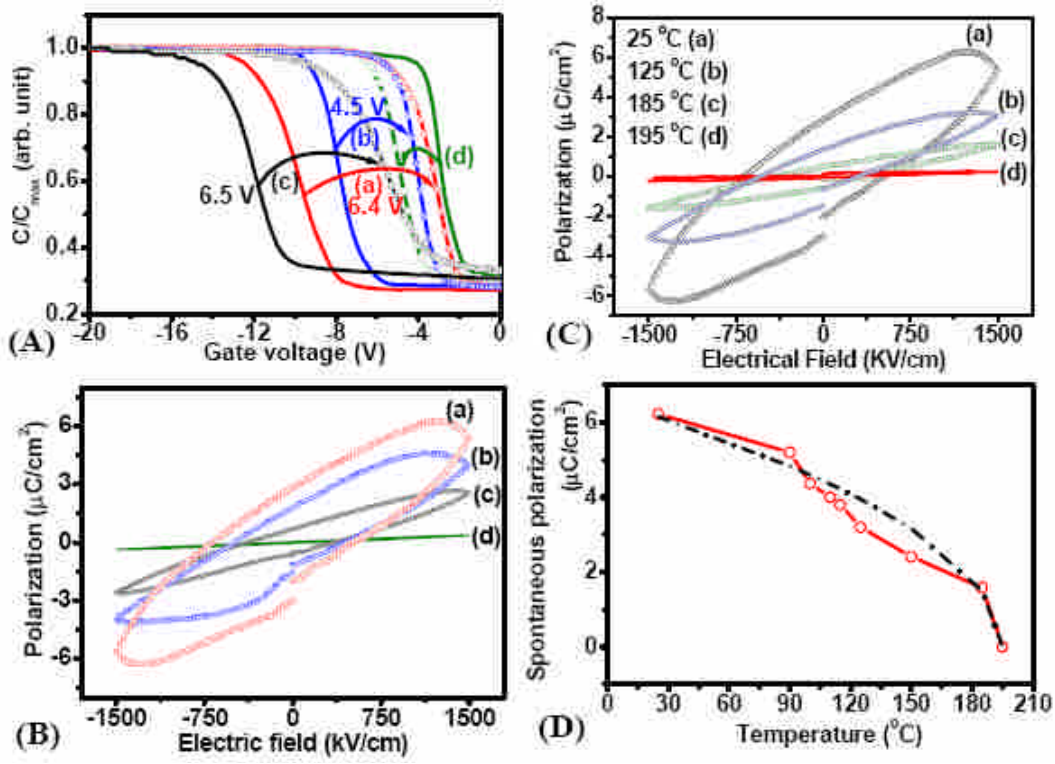


**Fig. I-3**: (A) C-V hysteresis characteristics of MOS capacitors containing an insulation layer of nc-Si embedded MS with high (curve *a* in red), moderate (*b* in blue), and low (*c* in black) densities of nc-Si (see text). C-V hysteresis curves for an annealed MS film with a moderate density of nc-Si (*d* in olive) are also shown for comparison. Solid and dashed lines represent C-V curves obtained in a positive (+V) to negative (–V) and negative (–V) to positive (+V) voltage sweeps, respectively. Sweeping ranges of bias voltage for the four cases were (+0 V, -20 V), (+0 V, -20 V), (+0 V, -20 V), and (+4 V, -12 V), respectively. (B) P-E hysteresis curves of the MOS capacitors as that were characterized in Fig. 3(A). (C): P-E hysteresis curves of MOS capacitors containing an insulation layer of nc-Si embedded MS measured at 25 °C (a), 125 °C (b), 185 °C (c), and 195 °C (d). (D): Temperature dependence of spontaneous polarization for the nc-Si embedded MS. The dash line is the fit to $P_s = K\sqrt{T_o - T}$.

The existence of electrical polarization in the nc-Si embedded MS structures can be revealed with P-E measurements. The results are presented in Fig. I-3 (B). The remnant polarizations $P_r$ of the three samples were found to be 3.0, 1.6, and 0.7 μC/cm$^2$, respectively and are much larger than the reported values for iron-passivated porous silicon (21). The measured remnant

polarizations correspond to an averaged dipole moment of ~$2.5x10^{-18}$ μC-cm for each nanocrystal. We estimate the number density of atoms in the ~1-nm thick hemispherical interface to be about $3.8x10^{15}cm^{-2}$ based on the structure of $SiO_2$/Si interface. To check, we note that integrated XPS peak area of Ge-O bonds is comparable to that of Ge-Ge (See Fig. I-2(A)). It indicates that there are about 300 heteropolar bonds lying in the hemispherical interface of one nanocrystal or a dipole layer of $5x10^{-18}$ μC-cm, which is about twice that of our P-E measurement.

According to the theoretical work by Miller and McWhorter (22), an electrical polarization higher than 0.1 $\mu C/cm^2$ is sufficient to switch the Si surface potential from depletion to inversion. Ferroelectricity-induced C-V memory window ($\Delta V$) can be determined from the coercive field ($E_c$) by $\Delta V=2E_c.d$ (20), where *d* denotes the thickness of ferroelectric films. For the sample with the lowest density of nc-Si, the C-V memory window was calculated to be about 6.6 V with a measured coercive field of 385 kV/cm. This agrees fairly well with the measured value of 6.5 V. However, for the samples with higher nc-Si density and therefore larger coercive field, the measured C-V memory windows were found to not monotonically increase with nc-Si density (or coercive field), indicating that the charging effect of quantum dots can not be neglected in the samples with high dot density. The remnant polarization also correlates well with the integrated area of the 460-nm PL peak. This supports the notion that the permanent dipole moments of our nanostructured films are related to the interfacial oxygen defects of nc-Si/silica arrays. The interfacial bonding structures are fairly stable with the resulting ferroelectric properties (spontaneous polarization $\boldsymbol{P_s}$) persisting up to 195°C (See Fig. I-3 (C-D)) (23). The phase transition is identified to be second order with a Curie temperature of $T_0$=195°C from a fit to $P_s=K(T_o-T)^{1/2}$ (2). The fairly good fit also implies that the dipole layers from the one-side bonding geometry couple to form one single ferroelectric domain in our nanostructured ferroelectric films.

In conclusion, we report a new class of non perovskite-type ferroelectric materials synthesized by embedding three-dimensional arrays of nc-Si (or nc-Ge) in mesoporous silica matrix. Its Curie-temperature is as high as 195 °C. Material characterizations indicated that the nanocrystals formed non-centrosymmetric bonding with the host silica matrix with highly stable interface structures, which exhibited the dipole effect at one-side bonded surfaces of Si (or Ge) nanocrystals with mesoporous silica matrix and caused one-tenth remnant polarization of typical perovskite ferroelectrics. The polar structure is verified by surface sum frequency spectroscopy. An effective second-order nonlinear coefficient of 3.8 pm/V is estimated. The resulting ferroelectricity in the polar nanostructure involves only silicon (or germanium) and oxygen atoms. This novel material thus promises potential applications for better and more compact non-volatile memories compatible with the standard CMOS process flow.

**References**


1. K. J. Choi, M. Biegalski, Y. L. Li, A. Sharan, J. Schubert, R. Uecker, P. Reiche, Y. B. Chen, X. Q. Pan, V. Gopalan, L.Q. Chen, D. G. Schlom, and C. B. Eom, *Science* **306**, 1005 (2004).
2. C. Kittel, Introduction to Solid State Physics (Wiley, New York, 1996), pp. 393-402.
3. N. A. Spaldin and M. Fiebig, *Science* **309**, 391 (2005).
4. P. Muralt, *J. Micromech. Microeng.* **10**, 136 (2000).
5. T. Li, S. T. Hsu, B. D. Ulrich, and D. R. Evans, *Appl. Phys. Lett.* **86**, 123513 (2005).
6. C. Y. Chang, and S. M. Sze, ULSI DEVICES (Wiley, New York, 2000), pp. 448-463.
7. C. H. Ahn, K. M. Rabe, and J. -M. Triscone, *Science* **303**, 488 (2004).

8. H. Yamada, Y. Ogawa, Y. Ishii, H. Sato, M. Kawasaki, H. Akoh, and Y. Tokura, *Science* **305**, 646 (2004).
9. H. Y. Fan, K. Yang, D. M. Boye, T. Sigmon, K. J. Malloy, H. F. Xu, G. P. López, and C. J. Brinker, *Science* **304**, 567 (2004).
10. D. Y Zhao, P. D. Yang, N. Melosh, J. G. Feng, B. F. Chmelka, and G. D. Stucky, Adv. Mater. 10, 1380 (1998).
11. A. T. Cho, J. M. Shieh, J. Shieh, Y. F. Lai, B. T. Dai, F. M. Pan, H. C. Ku, Y. C. Lin, K. J. Chao, and P. H. Liu, *Electrochem. Solid-State Lett.* **8**, G143 (2005).
12. Materials and methods are available as supporting material on *Science* Online.
13. Y. Zhang, F. Phillipp, G. W. Meng, L. D. Zhang, and C. H. Ye, J. Appl. Phys. **88**, 2169 (2000).
14. J. Y. Zhang, X. M. Bao, Y. H. Ye, and X. L. Tan, *Appl. Phys. Lett.* **73**, 1790 (1998).
15. M. V. Wolkin, J. Jorne, P. M. Fauchet, G. Allan, and C. Delerue, *Phys. Rev. Lett.* **82**, 197 (1999).
16. T. Baron, B. Pelissier, L. Perniola, F. Mazen, J. M. Hartmann, and G. Rolland, *Appl. Phys. Lett.* **83**, 1444 (2003).
17. Xingcai Su, L. Lianos, Y. Ron Shen, and Gabor A. Somorjai, *Phys. Rev. Lett.* **80**, 1533 (1998).
18. S. Tiwari, F. Rana, H. Hanafi, A. Hartstein, E. F. Crabbe´, and K. Chan, *Appl. Phys. Lett.* **68**, 1377 (1996).
19. J. K. Kim, H. J. Cheong, Y. Kim, J. Y. Yi, H. J. Bark, S. H. Bang, and J. H. Cho, *Appl. Phys. Lett.* **82**, 2527 (2003).
20. J. P. Han, S. M. Koo, C. A. Richter, and E. M. Vogel, *Appl. Phys. Lett.* **85**, 1439 (2004).
21. Q. Chen, X. Li, Y. Zhang, and Y. Qian, Adv. Mater. 14, 134 (2002).
22. S. L. Miller and P. J. McWhorter, *J. Appl. Phys.* **72**, 5999 (1992).
23. R. Moro, X. Xu, S. Yin, and W. A. de Heer, *Science* **300**, 1265 (2003).

**(II) ZnO nano building block as a molecular binder to improve the application properties of ferroelectric liquid crystal molecules**

Modifications of the electro-optical properties of an existing SSFLC by doping with appropriate impurities had recently attracted significant interest. Concerted efforts in nanostructured materials and LC technologies had been employed to demonstrate the potential to yield an improved LC alignment and EO properties. The developments had also revealed that the phase transition, elastic coupling, ionic effect, and dielectric anisotropy of LC materials are adjustable with doping of various nanomaterials, such as silica particles, LC-covered Pd particles, and ferroelectric nanoparticles, *etc*. The design parameters of the methodology include material, size and shape, doping concentration and surfactant properties of nanoparticles, which could open an effective and flexible way for generating promising new materials for the next generation LC flat panel display.

The molecular alignment of surface-stabilized ferroelectric liquid crystal (SSFLC) device with and without nc-ZnO doping is revealed in the angular distibution profiles of azimuthal and tilt angles as shown in Fig. II-1(a) and II-1(b) by using our patented imaging polarimetry technique. As shown below, we found doping of nc-ZnO can reduce the distribution width of SSFLC tilt angle by two times. The reduction effectively improves the optical transmission efficiency (see Fig. II-1(c)) and decreases light leakage in the dark state of an SSFLC device.

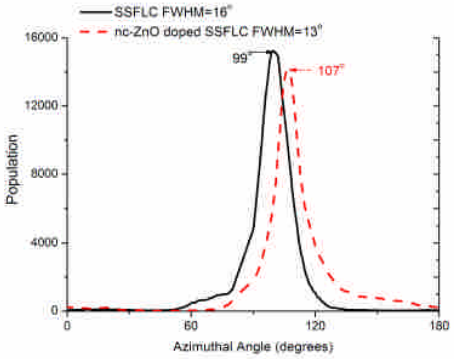


(a)

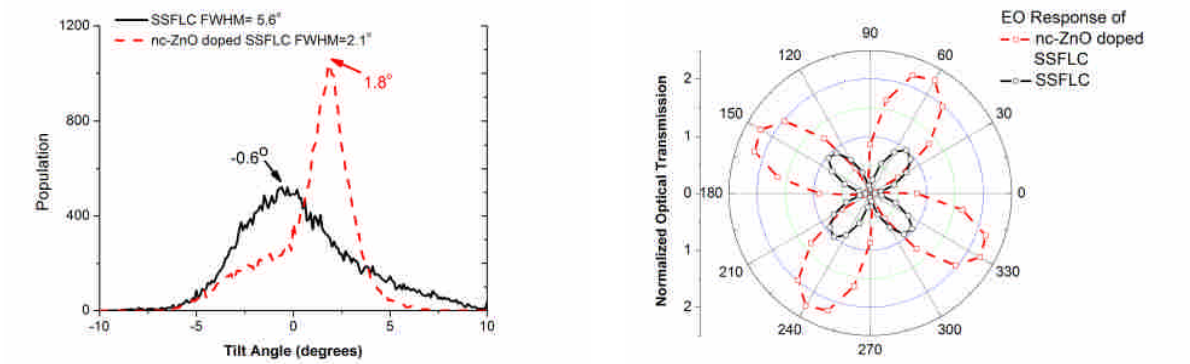


(b) (c)

**Figure II-1** The angular distribution of (a) the azimuthal angle, and (b) tilt angle of an SSFLC device with and without nc-ZnO doping. (c) The corresponding optical transmission azimuthal patterns of the SSFLC devices.

The dynamic optical transmission of an SSFLC inserted between a cross polarizer-analyzer setup can be depicted with $\bar{I}(\Phi)=b(t)+c(t)\cos^2\left[2\left(\Phi+\omega(t)\right)\right]$, where $b(t)$ denotes an isotropic part of the dynamic alignment of SSFLC, $c(t)=0.5\sin^2(\Gamma/2)$ represents the contribution of uniaxial alignment, and $\omega(t)$ is the azimuthal angle of the optic axis projected onto the cell substrate. Note that upon the reversal of the sign of an applied field, all the molecules in the ferroelectric phase switch by rotation about a tilt cone. Owing to the conic motion, $c(t)$ can vary with polar angle $\alpha$. The detailed information about the conic motion of SSFLC can be identified by analyzing the dynamic EO response patterns.

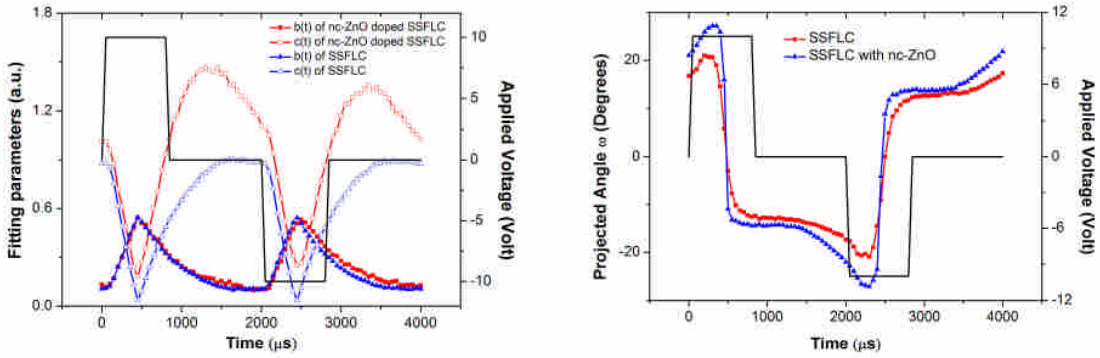


Fig. II-2 (a) Fitting parameters (symbols) of the EO azimuthal patterns and the applied voltage (solid line) are plotted as a function of time. (b) The deduced orientation angle of the optic axis of FLC film is shown. Rubbing direction of the FLC cell is along the 0 degree.

Figure II-2 presents the time-resolved electro-optical azimuthal patterns of undoped and nc-ZnO-doped SSFLC cells. The contrast ratio of the optical transmission decreases during the field-on period, as shown by a rapid increase of the isotropic component $b(t)$. The isotropic component then slowly decreases with an accompanying increase of $c(t)$.

It is surprising to find that $c(t)$ of SSFLC cell with ZnO nanocrystal doping increases significantly during switching as comparing with the SSFLC without nc-ZnO doping. ZnO nanocrystals used in this study provide a binding effect to FLC molecules and lead to an improved LC alignment quality both in steady-state and in dynamic processes as clearly revealed

in Figs. II-1 and II-2.

**(III) Solution grown core-shell quantum dots for building highly ordered self-assembling films**

Nanotechnology offers the possibility for tuning and enhancing application properties of materials and devices. This potential can be realized from the design and synthesis of nano building blocks to periodic structure assembly. Recently, we had implemented the concept into a technology platform suited for this project. Here I use Fe/Au core-shell quantum dot as an example to illustrate the essential concept. Fe/Au core-shell quantum dot itself is also attractive for its combined functionality of optics and magnetism. Au nanoshell can response significantly to an optical field from near infrared to ultraviolet spectrum, while the iron nano core generates ferromagnetic response to a magnetic field.

The synthesis process is briefly depicted in Fig. III-1, which starts from the synthesis of iron nano core with reverse micelle nanoreactor concept (step A). An Au nanoshell is then coated over the iron core. We modify the surfaces of the resulting core-shell quantum dots with 1-dodecanethiol for stabilizing the nanoparticles and then encapsulate the nano building blocks in surfactants to form water-soluble double layer. We can use the double layer thickness to control the interparticle separation in 3D structure. Finally at step E, TEOS molecules are added and attracted onto the hydrophilic surfaces of the core-shell quantum dots. TEOS molecules provide directive sol-gel process, which *glue* quantum dots together and result in a rigid periodic 3D structure.

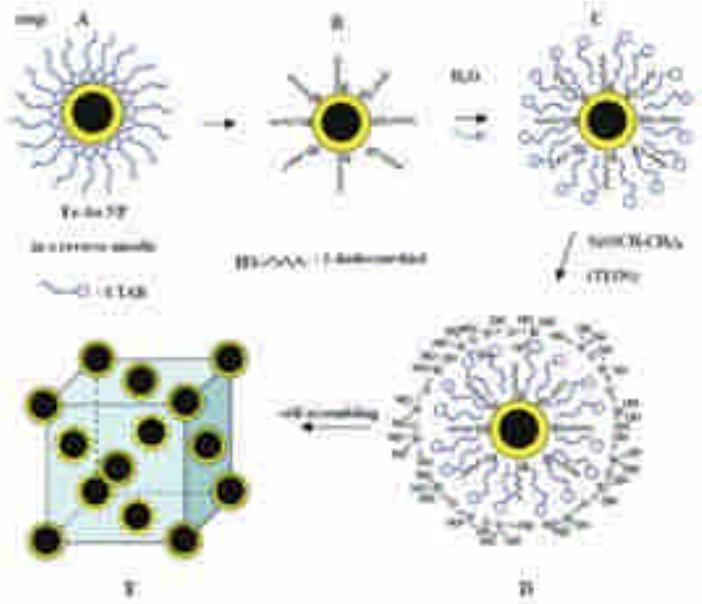

**Fig. III-1.** Schematic diagram showing the synthesis of water-soluble iron-gold core-shell nanoparticles: (A) The iron nano core is first synthesized with reverse micelle nanoreactor approach. (B) The Au nanoshell is then formed over the iron core. (C) The surface of the resulting core-shell quantum dot is then modified with 1-dodecanethiol. (D) The alkanethiol stabilized nanoparticles were encapsulated in surfactants to form water-soluble surface. (E) TEOS molecules are then attracted onto the hydrophilic surfaces of the core-shell quantum dots and direct the sol-gel process to combine quantum dots into periodic 3D structure.

We have verified experimentally the outcome of each step. By using the reverse micelle nanoreactor approach we can prepare metal or semiconductor quantum dots with particle size distribution less than 10%. Fig. III-2 exhibits a TEM picture of the Fe/Au nanoparticles with an

averaged size of 5.5 nm. The inset shows an enlarged picture with distinctive atomic planes, indicating an excellent crystalline quality of the core-shell quantum dots.

Another major concern of the technological platform is the ability to assemble artificial atoms into a robust 3D crystal. This is verified in Fig. III-2(b), where a HRTEM of a sample prepared at step E is presented. Clear atomic planes formed by these artificial atoms can be observed. This artificial crystal is identified to be fcc with X-ray diffraction.

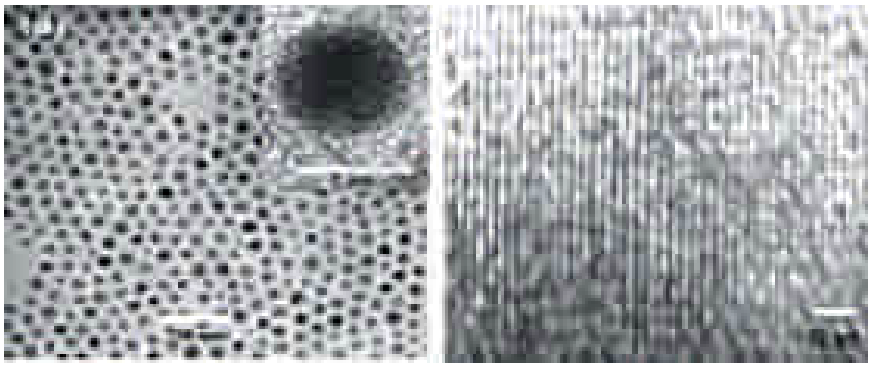

**Fig. III-2.** (a) TEM image of the Fe/Au core shell nanoparticles obtained after step D. The average size of these nanoparticles is 5.5nm with size deviation less than 1nm. (b) HRTEM of a sample prepared at step E is presented. X-ray diffraction pattern indicates this artificial crystal structure to be FCC.

The original motivation to assembly 3D artificial crystal with Fe/Au core-shell quantum dots is to investigate the magnetic response of the artificial crystal. Unfortunately, the averaged size of Fe/Au quantum dots is too small to yield stable magnetization above $10^{o}$K, thus these nanoparticles behave like super paramagnetic. In addition, the separation between two neighboring quantum dots are about 6 nm, which is too large to yield sufficiently large coupling for stable ferromagnetic phase. Nevertheless, the study up to this stage shows several advantages of using quantum dots in making artificial crystals. Firstly the lattice structure can be widely chosen and secondly interdot coupling and the properties of quantum dots can be separately modified.

Other applications of this technique include enhanced charge transport in CdSe quantum-dots (1) or nano rods embedded copolymer nanodomains (2), and enhanced photoluminiscent emission from $TiO_2$ nanocrystals embedded (3), or CdS QDs-embedded conjugate polymer (4).


(1). Chung-Ping Li, Kung-Hwa Wei and Jung Y. Huang, *Enhanced Collective Electron Transport by CdSe Quantum Dots Self-Assembled in the Poly(4-vinylpyridine) Nanodomains of a Poly(styrene-b-4-vinylpyridine) Diblock Copolymer Thin Film*, Angewandte Chemie International Edition 45, 1-5 (2006).

(2) Chung-Ping Li, Siao-Wei Yeh, Han-Chang Chang, Jung Y. Huang, and Kung-Hwa Wei, *The Orientation of CdSe Nanorods Affects the Electron Mobility of CdSe/P4VP Nanodomains Self-Assembled within a Poly(styrene-b-4-vinylpyridine) Diblock Copolymer Thin Film*, small 2006, 2, No. 3, 359 – 363 (2006, DOI: 10.1002/smll.200500399).

(3). Chin-Cheng Weng, Chia-Hung Chou, Kung-Hwa Wei1, and Jung Y. Huang , Enhanced Electroluminescence of Poly(2-methoxy-5-(20-ethylhexyloxy)-1,4-phenylene vinylene) Films in the Presence of TiO2 Nanocrystals, Journal of Polymer Research (2006, DOI: 10.1007/s10965-005-9030-x)

(4). Chia-Hung Chou, Hsu-Shen Wang, Kung-Hwa Wei and Jung Y. Huang, *Thiophenol-modified CdS nanoparticles enhance the luminescence of benzoxyl dendron-substituted polyfluorene copolymers*, Advanced Functional Materials (2005, in press).

**Conference paper to be presented in the 21st International Liquid Crystal Conference, Keystone, Colorado, USA, July 2-7, 2006.**

# *2D IR of sub molecular reorientation dynamics in surface stabilized ferroelectric liquid crystals with and without doping of ZnO nanocrystals*

Jung Y. Huang

Department of Photonics and Institute of Electro-Optical Engineering, Chiao Tung University

Hsinchu 305, Taiwan, Republic of China

Recently concerted efforts in nanostructured materials and LC technologies had been employed to demonstrate the phase transition, elastic coupling, ionic effect, and dielectric anisotropy of LC materials to be adjustable with doping of various nanomaterials. The design parameters of the methodology include material, size and shape, doping concentration and surfactant properties of nanoparticles, which open an effective and flexible way for generating promising new materials for the next generation LC flat panel display.

In this paper we report a two-dimensional infrared (2D IR) study of sub molecular reorientation in surface stabilized ferroelectric liquid crystals (SSFLC) with and without doping of ZnO nanocrystals. Time-resolved FTIR (trFTIR) spectra from 900 to 3500 $cm^{-1}$ with 4-$cm^{-1}$ resolution were recorded with a continuous-scan FTIR spectrometer equipped with a liquid nitrogen-cooled HgCdTe detector and home-made data acquisition electronics. Bipolar square-wave pulses were used to excite the SSFLC cells under test. For each polarization direction of the incident infrared light, a total of 32 time-resolved interferograms were acquired. The synchronous and asynchronous 2D correlation analysis with varying infrared polarization angles were calculated based upon an algorithm developed by Noda, and a software composed by S. Morita.

By using infrared two-dimensional correlation (2DC) and hetero-correlation (2DHC) techniques we first showed that the thermal fluctuations in the azimuthal angle of the FLC director about a tilted cone can be suppressed with an applied electric field. We then showed that the observed time courses of synchronous auto-peaks of 2DHC can be separated into three stages. In the stage I, the observed variations of angular spread are rapid with small amplitude. The observed hetero synchronous correlations exhibit nearly constant peak heights at the first 10 μsec, indicating that the relative angular motions start at the functional groups attaching to the same one molecule. In the stage II while the field is still applied, the hetero synchronous auto-peak heights begin to increase, indicating that the correlated motions propagate from the molecular fragments belonging to one molecule to those of other surrounding molecules. In stage III, slower but more significant variation in the hetero synchronous correlations were found and attributed to from the higher degrees of freedom in the field-induced intermolecular motion. The larger variation in the angular spread persists even after the applied field is switched off. We also applied the techniques to analyze the electro-optical switching of a ZnO nanocrystal (nc-ZnO)-doped SSFLC. An improved dynamic alignment and detailed information about sub molecular motion caused by nc-ZnO doping were revealed.

*We acknowledge the financial support from the National Science Council of the Republic of China under grant NSC 94-2112-M-009 -031 and Taiwan TFTLCD Association Foundation No. A623TT4000-V14.*